*remote sensing*

MDPI

*Article*

# Array Three-Dimensional SAR Imaging via Composite Low-Rank and Sparse Prior

**Zhiliang Yang [1], Yangyang Wang [1,2,*], Chudi Zhang [3], Xu Zhan [4], Guohao Sun [5], Yuxuan Liu [4] and Yuru Mao [1]**

[1] Shanxi Province Key Laboratory of Intelligent Detection Technology & Equipment, North University of China, Taiyuan 030051, China; yangzhiliang188@nuc.edu.cn (Z.Y.); 20160104@nuc.edu.cn (Y.M.)
[2] School of Aeronautics and Astronautics, University of Electronic Science and Technology of China, Chengdu 611731, China
[3] Intelligent Game and Decision Laboratory, Beijing 100091, China; zhangchd@mail2.sysu.edu.cn
[4] School of Information and Communication Engineering, University of Electronic Science and Technology of China, Chengdu 611731, China; zhanxu@std.uestc.edu.cn (X.Z.); eie.yuxuan.liu@std.uestc.edu.cn (Y.L.)
[5] School of Aeronautics and Astronautics, Sichuan University, Chengdu 611731, China; sgh2019@scu.edu.cn
* Correspondence: yangyangw@uestc.edu.cn

**Abstract:** Array three-dimensional (3D) synthetic aperture radar (SAR) imaging has been used for 3D modeling of urban buildings and diagnosis of target scattering characteristics, and represents one of the significant directions in SAR development in recent years. However, sparse driven 3D imaging methods usually only capture the sparse features of the imaging scene, which can result in the loss of the structural information of the target and cause bias effects, affecting the imaging quality. To address this issue, we propose a novel array 3D SAR imaging method based on composite sparse and low-rank prior (SLRP), which can achieve high-quality imaging even with limited observation data. Firstly, an imaging optimization model based on composite SLRP is established, which captures both sparse and low-rank features simultaneously by combining non-convex regularization functions and improved nuclear norm (INN), reducing bias effects during the imaging process and improving imaging accuracy. Then, the framework that integrates variable splitting and alternative minimization (VSAM) is presented to solve the imaging optimization problem, which is suitable for high-dimensional imaging scenes. Finally, the performance of the method is validated through extensive simulation and real data experiments. The results indicate that the proposed method can significantly improve imaging quality with limited observational data.

**Keywords:** three-dimensional (3D) imaging; synthetic aperture radar (SAR); alternative minimization; low-rank; non-convex

check for updates

Academic Editor: Fabio Rocca

Received: 3 December 2024
Revised: 8 January 2025
Accepted: 16 January 2025
Published: 17 January 2025

**Citation:** Yang, Z.; Wang, Y.; Zhang, C.; Zhan, X.; Sun, G.; Liu, Y.; Mao, Y. Array Three-Dimensional SAR Imaging via Composite Low-Rank and Sparse Prior. *Remote Sens.* **2025**, *17*, 321. https://doi.org/10.3390/rs17020321

**Copyright:** © 2025 by the authors. Licensee MDPI, Basel, Switzerland. This article is an open access article distributed under the terms and conditions of the Creative Commons Attribution (CC BY) license (https://creativecommons.org/licenses/by/4.0/).

## 1. Introduction

Synthetic aperture radar (SAR) imaging plays an increasingly important role in a variety of fields, such as terrain monitoring [1–3], target detection [4,5], and measurement of target scattering information [6–8], due to its ability to achieve effective imaging in extreme weather conditions. Traditional SAR imaging only obtains two-dimensional (2D) information regarding the real imaging space, lacking elevation information [9]. In complex urban or mountainous scenes, this can lead to the aliasing phenomenon. In addition, it is also difficult to eliminate the target distortion caused by multipath effects for 2D imaging [10].

In recent years, with the development of SAR systems, array three-dimensional (3D) SAR imaging has become one of the hotspots in the field of radar imaging [11–13]. The array 3D SAR achieves 3D resolution capability by synthesizing a 2D virtual array through the motion of the antenna platform, combined with range pulse compression. Different from 2D imaging, 3D imaging can obtain 3D information regarding the target space, thereby supporting application requirements such as 3D modeling of buildings and target scattering diagnosis [14,15]. At present, the methods for achieving 3D SAR imaging are classified into different types based on differences in basic principles. The first category of imaging method is to reconstruct the scene by utilizing the matched filtering (MF) principle based on full sampling. These methods only consider the system measurement model, and the imaging results are susceptible to interference such as noise and clutter. Additionally, such methods typically require observation data that satisfy the Nyquist sampling theorem to support imaging [16]. The second category is imaging methods based on the principle of sparse reconstruction. This type of method further considers the prior of the imaging scene and introduces the regularization function to characterize the target features, which can enhance the target features to a certain extent while suppressing noise and clutter [17,18].

From the perspective of Bayesian theory, sparse imaging is also a typical ill-posed inverse problem. Therefore, it is necessary to introduce regularization functions to achieve effective solutions and enhance target features. The typical sparse imaging model is constructed using the $L_1$ regularization function, which is utilized to characterize the sparse prior of the imaging space [19]. For SAR imaging, the earliest method used for prior representation is the introduction of the $L_1$ regularization function. In [20], the $L_1$ regularization function was introduced into complex approximate message passing (CAMP). The above method can suppress sidelobes and enhance the target-to-background ratio (TBR) in 2D SAR images. In [21], a method for airborne 3D SAR imaging that integrates the $L_1$ regularization and polar formatting was proposed, which can improve image defocusing caused by motion errors in airborne SAR systems, thereby enhancing imaging performance. Although imaging methods based on $L_1$ regularization functions can suppress noise and improve image quality to a certain extent, these methods may introduce bias effects in imaging [22,23]. Specifically, for SAR imaging scenarios, bias effects may lead to amplitude errors in reconstructed targets, which may reduce imaging accuracy and make it difficult to meet the needs of image interpretation [18,24]. Based on this, relevant scholars have studied more sophisticated non-convex regularization functions to mitigate the impact of bias effects. At present, non-convex regularization functions commonly used for SAR imaging include $L_q$ regularization functions [25,26], smooth clipped absolute deviation (SCAD) [27], the $L_{1/2}$ regularization function [28], and minimax convex penalty (MCP) [29]. By combining the proximal operator of non-convex regularization functions with proximal gradient descent methods, effective solutions to imaging problems can be achieved, leading to effective reconstruction of observation scenes, such as the iterative shrinkage and thresholding (IST) algorithm [30], the alternating direction method of multipliers (ADMM) algorithm [31,32], the approximate message passing (AMP) algorithm [33], the half-quadric splitting algorithm (HQS) [34], and generalized alternating projection (GAP) [35]. In [36], an improved method was developed to promote the imaging effect of Gaofen-3 data, which characterizes target sparsity prior through generalized minimax convolution (GMC). In [37], a SAR imaging method with $L_{2,1}$ regularization was developed to improve the reconstruction precision of spaceborne SAR. Compared with $L_1$, it can better suppress ghosts. In [38], an ISAR imaging method based on the $L_{1/2}$ regularization function and a threshold iterative algorithm was proposed to improve ISAR imaging performance. In [39], a polarimetric HoloSAR imaging method was proposed, which utilizes the structural correlation between echo data from different polarization channels to achieve imaging scene reconstruction.

In [40], by combining the $L_{1/2}$ regularization function and CAMP to improve ISAR imaging performance, it can suppress clutter in the image compared to MF. In [41], an imaging method based on the Cauchy regularization function and convex optimization techniques was developed to raise the quality of 3D imaging, which can alleviate the bias effect of the $L_1$ regularization function.

Though the above imaging methods promote imaging accuracy of SAR compared to imaging methods based on $L_1$ regularization functions, these methods only consider the sparse prior of the target scene, which is mainly point features. In the 3D imaging space, it is difficult to support the composite features of the target. Specifically, in 3D SAR imaging, there are non-sparse or non-smooth regions that can be characterized as low-rank structures, and imaging methods based on sparse drive can suppress such information in the target scene [42,43]. In 3D SAR imaging, the target scene may contain zones that do not have obvious sparsity (such as continuously distributed scatterers and irregular target surfaces), but these zones may still have low-rank features (such as highly correlated structural patterns). In these regions, sparse-driven imaging methods may suppress low-rank information, leading to a decrease in the quality of reconstruction results. Thus, introducing low-rank priors can help capture these features with inherent structure, rather than relying solely on sparsity [42,44]. Therefore, the above methods may lose target information in 3D SAR imaging scenes and limit imaging quality. The SAR images generated by such methods are not suitable for applications such as image interpretation. To address this issue, we construct an imaging optimization model based on composite priors, which provides feasibility for exploring the simultaneous introduction of sparse and low-rank priors (SLRP) in array 3D SAR scenes. In addition, traditional low-rank optimization problems use convex relaxation and nuclear norm to solve [45,46]. However, the nuclear norm has some drawbacks, as it imposes the same penalty on all singular values. Typically, larger singular values represent the main information in the image, while smaller singular values represent noise and clutter. Therefore, we expect to impose fewer penalties on larger singular values. Based on this, we construct an improved nuclear norm (INN) to achieve more reasonable penalties rather than treating all singular values equally, which can reduce bias estimation in imaging and improve imaging quality. Regarding the process of sparse echo data, apart from the framework of this article, which focuses on sparsity-based reconstruction that leverages the low-rank characteristics of targets to directly reconstruct imaging results from sparse data, there is another type being studied recently: the echo completion method. This approach contrasts with the sparsity-based reconstruction method by employing a two-stage process. In the first stage, it completes the sparse echo data by using techniques that exploit the low-rank properties of the echoes to generate a fully-sampled dataset. These completed data are then processed using standard matched-filtering methods, such as the Range Migration Algorithm (RMA), in the second stage. The sparsity-based reconstruction method effectively leverages target-specific features to enhance image quality, significantly minimizing artifacts such as sidelobes and clutter. Although it is somewhat sensitive to the chosen sparse sampling patterns, it generally achieves superior imaging outcomes. In contrast, the echo completion method offers greater stability across various sampling patterns; however, it tends to yield lower-quality images due to the inherent limitations of standard matched-filtering techniques in addressing noise and sidelobe effects.

The main contributions of this article are as follows. A novel method for 3D SAR imaging based on SLRP is proposed. Firstly, an imaging optimization model based on composite priors is constructed to explore composite features in 3D SAR scenes. The improved nuclear norm (INN) in the constructed model can further reduce bias effects and improve imaging quality. Secondly, in order to solve the imaging optimization problem based on the composite priors mentioned above, a framework that integrates variable

splitting and alternative minimization (VSAM) is presented, which can be adopted for high-dimensional imaging scenes. Compared with sparse driven methods, the proposed method can reconstruct imaging scenes with limited observation data while preserving the composite structure of the target. Additionally, the convincingness of the imaging method in this article is verified via extensive simulations and experiments, and the results indicate that the developed method reconstructs the target with limited observation data.

The remainder of this article is organized as follows. The typical imaging model of array 3D SAR is introduced in Section 2. The developed imaging method is illustrated in detail in Section 3. In Section 4, simulation and experimental results are provided and the performance of the proposed method is analyzed. Finally, the conclusion of this article is made in Section 5.

## 2. Typical Imaging Model of Array 3D SAR

The array resolution of SAR systems is usually achieved through a virtual 2D array. Transmitting broadband signals in the range direction achieves range resolution, thereby enabling three-dimensional imaging of the observation space. Figure 1a presents the typical experimental diagram of the SAR system. In the imaging space, the range direction is along the $X$-axis, while the array direction is along the YZ plane. The system emits a broadband linear frequency modulated (LFM) signal via the radar transmitting antenna. Then, the system receives echo signals from the imaging scene. The mathematical expression of the echo signal is as follows:

$$\mathbf{y}_{raw}(\mathbf{P},\tau) = \iiint_{\mathrm{P}_t\in\Omega} \sigma(\mathrm{P}_t)\exp\left\{-j\pi K\left(\tau-\frac{2R}{c}\right)^2\right\}\exp\left\{-j\frac{4\pi f}{c}R\right\}d\mathrm{P}_t \tag{1}$$

where $\mathbf{y}_{raw}$ is the echo signal of the observation space, $\Omega$ is the observation space, P is the position of the array elements, and $\mathrm{P}_t$ is the location of the scattering point on target. $f$, $c$, and $\tau$ are the signal carrier frequency, the speed of light, and fast time, respectively. $R$ is the distance history between the array elements and scattering unit of the target,

After pulse compression of range, the echo takes the following form:

$$\mathbf{y}_r(\mathbf{P},r) = \iiint_{\mathrm{P}_t\in\Omega_r} \sigma(\mathrm{P}_t)\sin c(r)\exp\left\{-j\frac{4\pi f}{c}R\right\}\mathrm{dP}_t \tag{2}$$

where $\sin c(r)$ represents the range envelope, $\sigma$ represents the scattering coefficient, and $r$ represents the unit index in the range direction.

When performing subsequent imaging processing on the signal, its discrete form is required and the corresponding discrete form of (2) is:

$$\mathbf{y}_{rs}(\mathbf{P},r) = \sum_{\mathrm{P}_t\in\Omega_r} \nu(\mathrm{P}_t)\exp\{-j2kR\} \tag{3}$$

where $\nu(\mathrm{P}_t) = \sigma(\mathrm{P}_t)\sin c(r)$. Based on the above signal model, the corresponding linear model is further obtained:

$$\mathbf{y} = \mathbf{A}\mathbf{x} + \mathbf{n} \tag{4}$$

where $\mathbf{y} \in C^{Q\times 1}$ represents the echo signal, $\mathbf{A} \in C^{Q\times S}$ represents the observation matrix of the system, $\mathbf{x} \in C^{S\times 1}$ represents the scattering coefficient of the imaging area, and $\mathbf{n} \in C^{Q\times 1}$ represents noise.

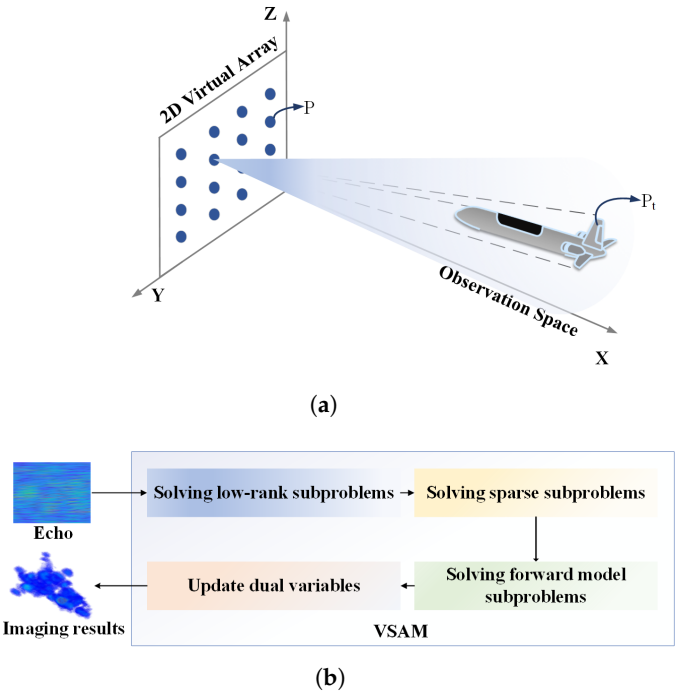



**Figure 1.** Imaging model and flowchart. (**a**) Geometric diagram of array 3D SAR imaging. (**b**) Process flowchart of the proposed method.

The imaging method based on MF only considers the system observation matrix and does not utilize the prior information of the target in 3D space, making it susceptible to noise interference and difficult to achieve effective reconstruction with limited observation data. Compared with the above methods, imaging methods based on sparse reconstruction further introduce target priors, which can significantly improve image quality [47]. Based on the Bayesian criterion, the sparse SAR imaging problem is equivalently treated as a maximum-a-posteriori estimation problem.

$$\begin{aligned}\hat{\mathbf{x}} &= \arg\max_{\mathbf{x}} P(\mathbf{y}|\mathbf{x})P(\mathbf{x})/P(\mathbf{y}) \\ &= \arg\min_{\mathbf{x}} -\log P(\mathbf{y}|\mathbf{x}) - \log P(\mathbf{x}) \\ &= \arg\min_{\mathbf{x}} f(\mathbf{x}) + \lambda\eta(\mathbf{x})\end{aligned} \tag{5}$$

Since $P(\mathbf{y})$ is independent of $\mathbf{x}$, it can be ignored. In SAR imaging, $f(\mathbf{x}) = -\log P(\mathbf{y}|\mathbf{x})$ represents the data fidelity term. $\eta(\mathbf{x}) = -\log P(\mathbf{x})/\lambda$ represents a prior term, which is usually a regularization function of different types.

By introducing the $L_1$ regularization function, we can obtain the corresponding typical imaging optimization model:

$$\hat{\mathbf{x}} = \arg\min_{\mathbf{x}} \left\{ \frac{1}{2}\|\mathbf{y} - \mathbf{A}\mathbf{x}\|_2^2 + \lambda\eta_{L_1}(\mathbf{x}) \right\} \tag{6}$$

where $\eta_{L_1}(\cdot)$ represents the $L_1$ regularization function, and its corresponding proximal operator is as follows:

$$\varphi_{\lambda,L_1}(x_i) = \begin{cases} x_i - \lambda, & x_i \geq \lambda \\ 0, & |x_i| < \lambda \\ x_i + \lambda, & x_i \leq -\lambda \end{cases} \tag{7}$$

where $x_i$ is the i-th element of $\mathbf{x}$.

## 3. Array 3D SAR Imaging Based on Composite Prior

In this section, SAR imaging with solely sparse-driven methods is first introduced, and its problems in 3D SAR imaging are elaborated. Subsequently, in response to the aforementioned issues, the proposed 3D SAR imaging method based on composite priors with VSAM (CP-VSAM) is further elaborated, including the construction of an imaging optimization model and the corresponding solution framework, to achieve effective 3D imaging.

### *3.1. Imaging Based on Sparse Driven*

Sparse driven SAR imaging typically introduces a regularization function to characterize sparse features of the target, and the imaging task can be established as a corresponding constrained optimization problem:

$$\begin{aligned} &\min_{\mathbf{x}} f(\mathbf{x}) + \lambda\eta(\mathbf{u}) \\ &\text{subject to } \mathbf{x} = \mathbf{u} \end{aligned} \tag{8}$$

In order to solve the above optimization problem, it is necessary to establish its corresponding Lagrange objective function:

$$L(\mathbf{x}, \mathbf{u}, \mathbf{d}) = f(\mathbf{x}) + \lambda\eta(\mathbf{u}) + \frac{T}{2}\|\mathbf{x} - \mathbf{u} - \mathbf{d}\|_2^2 \tag{9}$$

where $\mathbf{d}$ and $T$ are dual variables and penalty parameters, respectively, and $\eta(\cdot)$ is a regularization function.

Taking SCAD as an example, the corresponding imaging optimization model is provided:

$$\begin{aligned} &\min_{\mathbf{x}} \tfrac{1}{2}\|\mathbf{y} - \mathbf{A}\mathbf{x}\|_2^2 + \lambda\eta_{SCAD}(\mathbf{u}) \\ &\text{subject to } \mathbf{x} = \mathbf{u} \end{aligned} \tag{10}$$

where $\eta_{SCAD}(\cdot)$ is the non-convex regularization function SCAD, and its expression is as follows:

$$\lambda\eta_{SCAD}(x_i) = \begin{cases} \lambda|x_i|, & |x_i| \le \lambda \\ \frac{-x_i^2 + 2\theta\lambda|x_i| - \lambda^2}{2(\theta-1)}, & \lambda < |x_i| \le \theta\lambda \\ (\theta+1)\lambda^2/2, & |x_i| > \theta\lambda \end{cases} \tag{11}$$

where $\theta > 2$. The proximal operator corresponding to SCAD is

$$\psi_{SCAD}(y_i; \lambda) = \begin{cases} \max(|y_i| - \lambda, 0)sign(y_i), & |y_i| \le 2\lambda \\ \frac{(\theta-1)y_i - \theta\lambda sign(y_i)}{\theta-2}, & 2\lambda < |y_i| \le \theta\lambda \\ y_i, & |y_i| > \theta\lambda \end{cases} \tag{12}$$

By incorporating proximal operators into gradient descent frameworks, optimization problems can be solved. Compared with imaging methods using the the $L_1$ regularization function, imaging methods using SCAD suppress the bias introduced by $L_1$ to a certain extent and improve the reconstruction accuracy. However, in 3D SAR imaging scenes, it only represents the sparse point-like features of the target, losing the non-sparse structural information of the target in space. To address this issue, we explore an array SAR imaging model based on composite priors, which combines SLRP while reconstructing the sparse and low-rank structure of the target to further improve the SAR imaging quality.

### *3.2. Array 3D SAR Imaging Based on Composite Priors*

The details of the array 3D SAR imaging method based on composite priors are illustrated. Firstly, the low-rank characteristics of the SAR image are analyzed, and the energy percentage (EP) is used to illustrate the low-rank nature of the SAR image.

$$EP(m) = \frac{\sum_{v=1}^{m} \|S_v\|^2}{\sum_{v=1}^{V} \|S_v\|^2} \tag{13}$$

where $S_v$ is the singular value of the image matrix, $V$ is the total number of singular values, and $m$ represents the top $m$ singular values with the highest values. From Figure 2, it can be seen that 6% of singular values capture 90% of the energy, indicating the low-rank of SAR image.

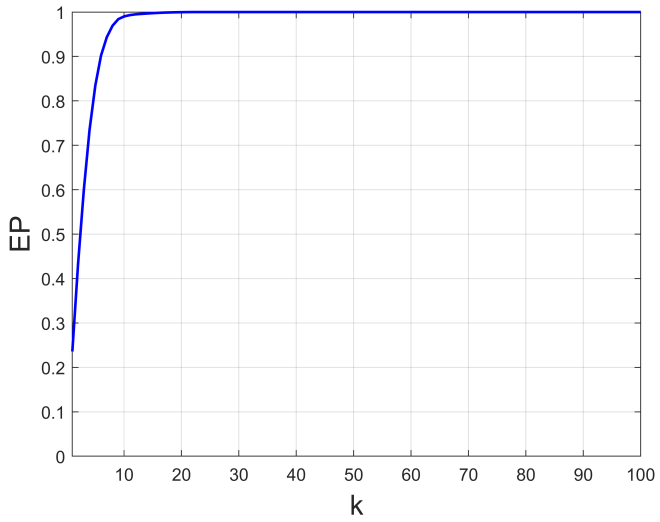



**Figure 2.** The low-rank of SAR image.

Then, by introducing imaging operators $I(\cdot)$ and the inverse operators $G(\cdot)$ [48], corresponding imaging models can be obtained:

$$\mathbf{y} = \mathbf{A}G(\mathbf{X}) + \mathbf{n} \tag{14}$$

where $\mathbf{X}$ is the matrix form of the SAR scene scattering coefficient, which includes two parts, namely, the low-rank part $\mathbf{L}$ and the sparse part $\mathbf{S}$.

The imaging optimization model based on composite prior is as follows:

$$\begin{aligned} &\min_{\mathbf{L},\mathbf{S}} \tfrac{1}{2}\|\mathbf{y} - \mathbf{A}G(\mathbf{X})\|_2^2 + \lambda_1\|\mathbf{L}\|_* + \lambda_2\|\mathbf{S}\|_1 \\ &\text{subject to } \mathbf{X} = \mathbf{L} + \mathbf{S} \end{aligned} \tag{15}$$

where $\mathbf{L}$ is the low-rank part of matrix $\mathbf{X}$, and $\mathbf{S}$ is the sparse part of matrix $\mathbf{X}$; $\|\cdot\|_*$ is the nuclear norm, which is a convex relaxation approximation of low-rank prior; and the $L_1$ regularization function $\|\cdot\|_1$ represents the sparse prior.

However, the $L_1$ regularization function in the above imaging model can introduce significant biases which adversely affect the reconstruction process and result in increased reconstruction errors for target amplitudes. Furthermore, the traditional nuclear norm applies imbalanced penalties to singular values due to convex relaxation during optimiza-

tion, leading to suboptimal imaging quality. Based on this, we constructed an imaging optimization model using non-convex regularization functions and INN.

$$\begin{aligned} &\min_{\mathbf{L},\mathbf{S}} f_1(\mathbf{X}) + \lambda_1 \eta(\mathbf{L})_{M,*} + \lambda_2 \eta(\mathbf{S})_{MCP} \\ &\text{subject to } \mathbf{X} = \mathbf{L} + \mathbf{S} \end{aligned} \tag{16}$$

where $f_1(\mathbf{X}) = \frac{1}{2}\|\mathbf{y} - \mathbf{A}G(\mathbf{X})\|_2^2$. $\eta(\cdot)_{M,*}$ represents the INN, and $\lambda_1$ and $\lambda_2$ are regular parameters. $\eta(\cdot)_{MCP}$ represents MCP, and the expression is as follows:

$$\eta_{MCP}(\mathbf{s}_i) = \begin{cases} \left(|\mathbf{s}_i| - \frac{|\mathbf{s}_i|^2}{2\gamma}\right), & |\mathbf{s}_i| \le \gamma \\ \frac{\gamma}{2}, & |\mathbf{s}_i| > \gamma \end{cases} \tag{17}$$

where $\gamma > 1$. $\mathbf{s}_i$ is an element in matrix $\mathbf{S}$.

The overall Lagrangian objective function corresponding to the imaging problem is given as

$$L_A(\mathbf{X}, \mathbf{L}, \mathbf{S}) = f_1(\mathbf{X}) + \lambda_1 \eta(\mathbf{L})_{M,*} + \lambda_2 \eta(\mathbf{S})_{MCP} + \langle \mathbf{D}, \mathbf{X} - \mathbf{L} - \mathbf{S} \rangle + \frac{\mu}{2}\|\mathbf{X} - \mathbf{L} - \mathbf{S}\|_F^2 \tag{18}$$

where $\mathbf{D}$ is Lagrange multipliers, and $\mu$ is the penalty parameter.

The above optimization problem is decoupled into multiple sub-problems through alternative minimization and solved in parallel, as shown in Figure 1b. Each sub-problem fixes the remaining variables, achieving the solution of a single variable.

$$\mathbf{L}^k = \arg\min_{\mathbf{L}} \lambda_1 \eta(\mathbf{L})_{M,*} + \left\langle \mathbf{D}^{k-1}, \mathbf{X}^{k-1} - \mathbf{L} - \mathbf{S}^{k-1} \right\rangle + \frac{\mu}{2}\left\|\mathbf{X}^{k-1} - \mathbf{L} - \mathbf{S}^{k-1}\right\|_F^2 \tag{19}$$

$$\mathbf{S}^k = \arg\min_{\mathbf{S}} \lambda_2 \eta(\mathbf{S})_{MCP} + \left\langle \mathbf{D}^{k-1}, \mathbf{X}^{k-1} - \mathbf{L}^k - \mathbf{S} \right\rangle + \frac{\mu}{2}\left\|\mathbf{X}^{k-1} - \mathbf{L}^k - \mathbf{S}\right\|_F^2 \tag{20}$$

$$\mathbf{X}^k = \arg\min_{\mathbf{X}} f_1(\mathbf{X}) + \left\langle \mathbf{D}^{k-1}, \mathbf{X} - \mathbf{L}^k - \mathbf{S}^k \right\rangle + \frac{\mu}{2}\left\|\mathbf{X} - \mathbf{L}^k - \mathbf{S}^k\right\|_F^2 \tag{21}$$

Let $\Gamma = \mathbf{X}^{k-1} - \mathbf{S}^{k-1} + \mathbf{E}^{k-1}$ and $\mathbf{E} = \frac{1}{\mu}\mathbf{D}$ be scaled Lagrange multipliers, then solve subproblem (19) by performing singular value decomposition (SVD) on $\Gamma$ and using the MCP proximal operator to penalize singular values. Singular values of $\Gamma$ can be achieved through SVD decoupling

$$\mathbf{U}_{k-1}\mathbf{\Lambda}\mathbf{V}_{k-1}^H = SVD(\Gamma) \tag{22}$$

where the diagonal element of $\mathbf{\Lambda}$ is the singular value $z$ of $\Gamma$. Then, further integrate the MCP proximal operator to solve for

$$\mathbf{L}^k = \mathbf{U}_{k-1} P_{MCP}(\mathbf{\Lambda}) \mathbf{V}_{k-1}^H \tag{23}$$

where $P_{MCP}(\cdot)$ is the MCP proximal operator, expressed as

$$P_{MCP}(z) = \begin{cases} 0, & |z| \le \lambda_2 \\ \gamma sign(z)\frac{|z| - \lambda_2}{\gamma - 1}, & \lambda_2 < |z| \le \lambda_2 \gamma \\ z, & |z| > \lambda_2 \gamma \end{cases} \tag{24}$$

Sub-problem (20) can be solved using non-convex regularization functions and the proximal operators. In this article, MCP is integrated to solve it

$$\mathbf{S}^k = P_{MCP}\left(\mathbf{X}^{k-1} - \mathbf{L}^k + \mathbf{E}^{k-1}\right) \tag{25}$$

Sub-problem (21) belongs the quadratic problem, which usually uses least squares to achieve effective solutions. However, it can lead to multidimensional matrix inversion operations, which is not applicable for 3D SAR imaging scenes. Therefore, we present an improved solution method. By linearizing sub-problem (21) and combining it with imaging operators, the solving process is further improved as

$$\mathbf{X}^k = \mathbf{X}^{k-1} - T\left[(\mu+1)\mathbf{X}^{k-1} - I(\mathbf{y}) - \mu\left(\mathbf{L}^k + \mathbf{S}^k - \mathbf{E}^{k-1}\right)\right] \tag{26}$$

where $T$ is the step factor.

Finally, it is necessary to update the scaled Lagrange multipliers:

$$\mathbf{E}^k = \mathbf{E}^{k-1} - \left(\mathbf{X}^k - \mathbf{L}^k - \mathbf{S}^k\right) \tag{27}$$

Based on the above process, parallel decoupling solution is applied to the sub-problems to achieve 3D imaging of the target region. The basic steps of the imaging method in this article are given in Algorithm 1. The proposed method can effectively preserve the information of the target in the presence of limited observational data by constructing LRSP. Firstly, in 3D SAR imaging, the data obtained by the sensor is usually a high-dimensional matrix containing reflected signals at different angles. The reflection information of the target object usually has some structural or common characteristics, manifested as a low-rank matrix. The low-rank characteristic enables the decomposition of high-dimensional data into multiple low-rank matrices, thereby reducing noise components in the data. The information of the target, such as shape and surface features, is usually located in the first few components of the low-rank matrix, while the noise component is removed. The main information can be extracted through low-rank decomposition techniques such as SVD or matrix completion. Secondly, in the process of SAR imaging, sparsity prior helps extract the most representative parts of the target features from the observed data, removing unimportant details or redundant parts. By sparsification, details of the target can be accurately restored, such as point features and textures. In the composite model, the global shape of the target is described by the low-rank part, while the local textures and details are captured by the sparse part. Thus, the proposed method achieves the preservation of target information in imaging scenes. Additionally, for parameter selection, we adopt a two-stage strategy, which has been adopted by past works, including our previous research. Specifically, we first select a rough parameter range based on experience, and then use the Bayesian information criteria (BIC) to further select appropriate parameters [49,50]. This parameter selection also helps to ensure the synergistic optimization of the performance of the different components for target recovery. For more sophisticated parameter tuning, strategies such as data-driven reinforcement learning [51], multi-scale optimization based on image-quality metrics [52], or multi-agent consensus equilibrium [53] can be explored in future work.

Next, convergence analysis is provided. The overall objective function expression is shown in (18). When the objective function satisfies the following inequality, the method converges:

$$L_A\left(\mathbf{X}^k, \mathbf{L}^k, \mathbf{S}^k\right) \leq L_A\left(\mathbf{X}^{k-1}, \mathbf{L}^{k-1}, \mathbf{S}^{k-1}\right) \tag{28}$$

**Proof.** In the optimization process, we decouple the optimization problem into three suboptimization problems to be solved in parallel. Therefore, the validity of the above equation depends on the convexity of each subproblem. The first two subproblems ((19) and (20)) are related to MCP. Under certain conditions $\gamma \geq \lambda$, MCP can retain convexity,

so the suboptimization problem is also convex [36,43]. $\gamma$ and $\lambda$ are the coefficients and regularization parameters of MCP, respectively.

The third subproblem (21) is a classical convex quadratic optimization problem, as described earlier in this manuscript, and the classical solution method for this type of problem is least squares. The update of each subproblem aims to iteratively minimize the objective function within the solving framework while keeping other variables fixed. Therefore, the following relationship holds, where each inequality is associated with the sequential variable updates:

$$L_A\left(\mathbf{X}^k, \mathbf{L}^k, \mathbf{S}^k\right) \leq L_A\left(\mathbf{X}^{k-1}, \mathbf{L}^k, \mathbf{S}^k\right) \leq L_A\left(\mathbf{X}^{k-1}, \mathbf{L}^k, \mathbf{S}^{k-1}\right) \leq L_A\left(\mathbf{X}^{k-1}, \mathbf{L}^{k-1}, \mathbf{S}^{k-1}\right) \quad (29)$$

□

**Algorithm 1:** The Basic Steps of CP-VSAM

**Input**:

Error parameter $\varepsilon$; $k^0 = 1$; Maximum number of iterations $k^{\max}$; $\mathbf{L}^0$; $\mathbf{S}^0$; $\mathbf{X}^0$; $\mathbf{E}^0$.

**While** $k \leq k^{\max}$ **and** Resi $> \varepsilon$

**Solve** $\mathbf{L}^k$

Equation (23)

**Solve** $\mathbf{S}^k$

Equation (25)

**Solve** $\mathbf{X}^k$

Equation (26)

**Solve** $\mathbf{E}^k$

Equation (27)

**Calculate the residual**

$\text{Resi} = \left\|\mathbf{X}^k - \mathbf{X}^{k-1}\right\|_F \Big/ \left\|\mathbf{X}^{k-1}\right\|_F$

$k = k + 1$

**Output**:

3D imaging results

## 4. Experiment and Analysis

Various simulations and actual experiments were conducted to investigate the imaging performance of CP-VSAM in different scenarios. To verify the effectiveness of CP-VSAM with different sampling rate (SR) and signal-to-noise ratios (SNR) conditions, a simulation experiment for a complex target was designed. Afterwards, real SAR imaging experiments were conducted to analyze the performance of CP-VSAM in real scenes. To evaluate and compare the performance of different methods, including the standard MF-type range migration algorithm without windowing, the $L_1$ method, SCAD, traditional low-rank and sparse methods, and the (LR-$L_1$) method, we used the following indicators: normalized mean square error (NMSE), structural similarity index measure (SSIM), and peak signal-to-noise ratio (PSNR).

The expression for NMSE is as follows:

$$\text{NMSE}(\hat{\mathbf{X}}, \mathbf{X}) = 20\log_{10}\frac{\left\|\hat{\mathbf{X}} - \mathbf{X}\right\|_F^2}{\|\mathbf{X}\|} \quad (30)$$

where $\hat{\mathbf{X}}$ and $\mathbf{X}$ are, respectively the, reconstructed image and the reference image.

The expression for SSIM is as follows:

$$\mathrm{SSIM}(\hat{\mathbf{X}}, \mathbf{X}) = \frac{(2\mu_1\mu_2 + C_1^2)(2\theta_{\hat{\mathbf{X}}\mathbf{X}} + C_2^2)}{(\mu_1^2 + \mu_2^2 + C_1^2)(\theta_1^2 + \theta_2^2 + C_2^2)} \tag{31}$$

where $\mu_1$ and $\theta_1$ denote the mean and the standard deviations of $\hat{\mathbf{X}}$, respectively; $\mu_2$ and $\theta_2$ denote the mean and the standard deviations of $\mathbf{X}$, respectively; $\theta_{\hat{\mathbf{X}}\mathbf{X}}$ denotes the cross-covariance; and $C_1$ and $C_2$ represent constants.

The expression for PSNR is as follows:

$$\mathrm{PSNR}(\hat{\mathbf{X}}, \mathbf{X}) = 10\log_{10}\frac{{L_r}^2}{\|\hat{\mathbf{X}} - \mathbf{X}\|_2^2} \tag{32}$$

where $L_r$ denotes the range of pixel values.

### *4.1. The Simulation of Aircraft Target*

The 3D imaging simulation of complex targets was implemented to evaluate the effectiveness of CP-VSAM in complex scenarios. The key parameters of the experimental setup are given below. The carrier frequency of the signal was 37.5 GHz; the bandwidth of the signal was 0.16 GHz; and the scanning range of the array set in the experiment was 3 m × 3 m.

Figures 3–5 presents the 3D SAR image of MF, $L_1$, SCAD, LR-$L_1$, and the proposed method at different SR. The image obtained by target extraction processing under full sampling echo was used as the reference image (RI), as shown in Figure 3a The visual images of different conditions show that the results based on MF with window (MFW) also had significant sidelobes under full sampling conditions.

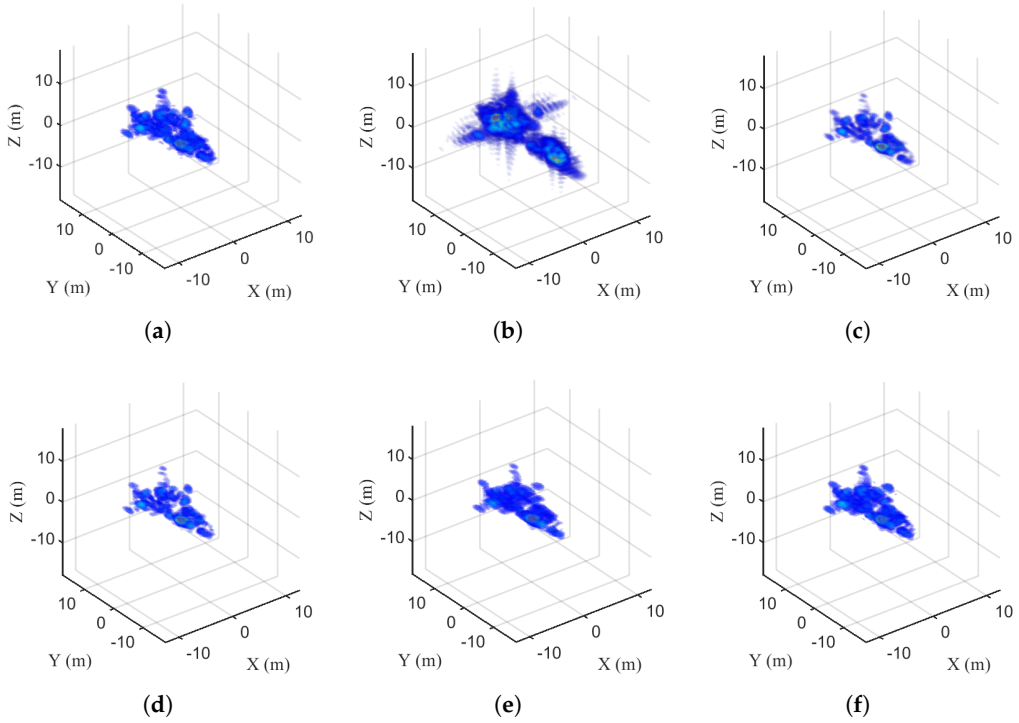



**Figure 3.** Aircraft target imaging results under 100% SR. (**a**) RI. (**b**) MFW. (**c**) $L_1$. (**d**) SCAD. (**e**) LR-$L_1$. (**f**) The proposed method.

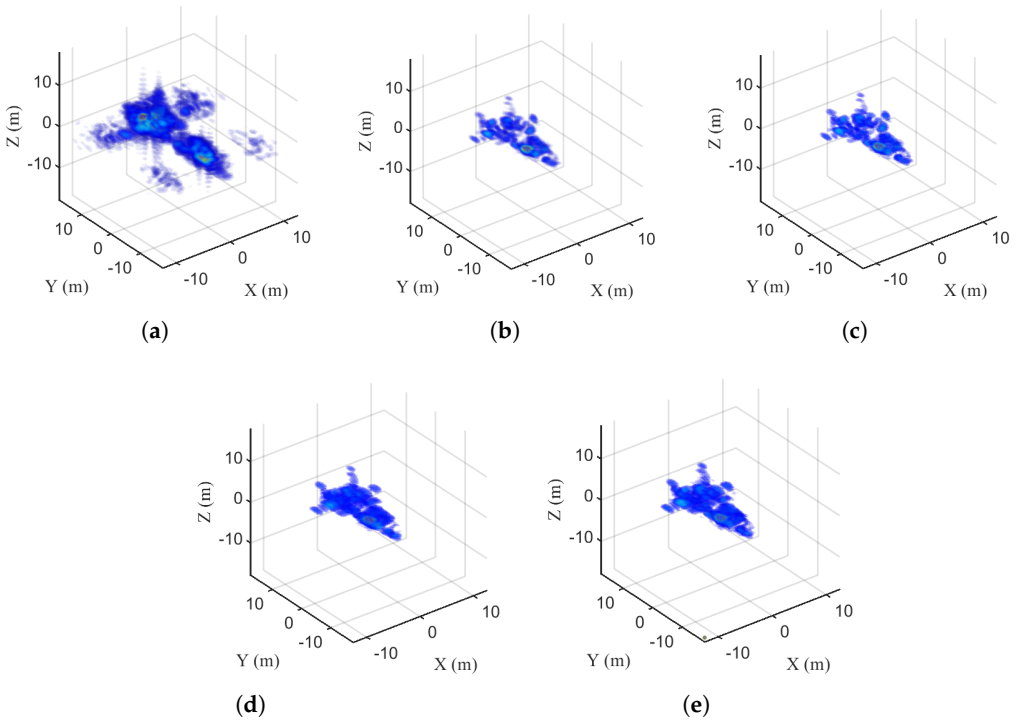



**Figure 4.** Aircraft target imaging results under 75% SR. (**a**) MFW. (**b**) $L_1$. (**c**) SCAD. (**d**) LR$-L_1$. (**e**) The proposed method.

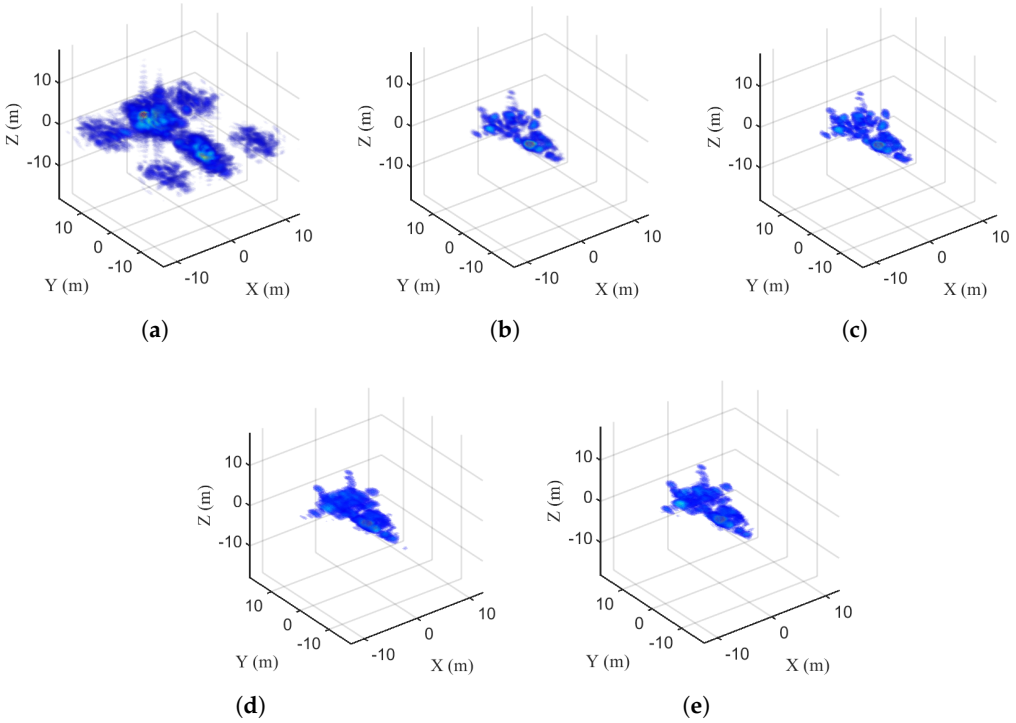



**Figure 5.** Aircraf target imaging results under 50% SR. (**a**) MFW. (**b**) $L_1$. (**c**) SCAD. (**d**) LR$-L_1$. (**e**) CP-VSAM.

As the amount of observed data decreased, the sidelobes in the imaging results based on MFW became more severe, and in some cases, grating lobes appeared. Therefore, it is challenging to accommodate the exigencies of high-quality imaging with this type of method. Compared with MFW, an imaging method based on sparse driving can effectively suppress sidelobes and improve imaging quality to a certain extent even in incomplete

data. However, this type of method only considers the sparse prior of the target, and in the 3D imaging space will lose target information as a result, affecting the imaging quality. Compared with the above methods, CP-VSAM effectively preserves the composite structure of the target and enhances the imaging quality.

Table 1 presents the quantitative evaluation indicators for various methods. At 75% sampling, the NMSE of $L_1$, SCAD, LR-$L_1$, and CP-VSAM were 0.3623, 0.1923, 0.1395, and 0.0695, respectively. The SSIMs of $L_1$, SCAD, LR-$L_1$, and CP-VSAM were 0.8931, 0.9284, 0.9871, and 0.9871, respectively. At 50% sampling, the NMSE of CP-VSAM was only 0.1026, and the SSIM was 0.9796. The results indicate that, even with incomplete observation data, the proposed method outperformed both $L_1$ and SCAD. It effectively enhances the quality of 3D SAR imaging, demonstrating its superiority.

**Table 1.** The NMSE and SSIM for aircraft imaging under varying SR conditions.

| SR | $L_1$ | | | SCAD | | | LR$-L_1$ | | | CP-VSAM | | |
|---|---|---|---|---|---|---|---|---|---|---|---|---|
| | NMSE | SSIM | PSNR | NMSE | SSIM | PSNR | NMSE | SSIM | PSNR | NMSE | SSIM | PSNR |
| 100% | 0.3410 | 0.9139 | 42.3109 | 0.1664 | 0.9475 | 45.7484 | 0.1286 | 0.9785 | 46.4850 | 0.0466 | 0.9914 | 47.6916 |
| 75% | 0.3623 | 0.8931 | 41.5266 | 0.1923 | 0.9284 | 44.1619 | 0.1395 | 0.9726 | 45.6716 | 0.0695 | 0.9871 | 47.0755 |
| 50% | 0.4002 | 0.8568 | 40.5834 | 0.2364 | 0.8965 | 43.5303 | 0.1505 | 0.9660 | 44.7753 | 0.1026 | 0.9796 | 46.6941 |

Subsequently, we conducted an in-depth analysis of the method's performance across different SNR. Specifically, Figure 6 illustrates the imaging outcomes of various methods at an SNR of 10 dB, while Figure 7 presents the corresponding results at an SNR of 5 dB. The visualization results indicate that traditional methods based on MFW are more sensitive to noise and the images may appear blurry. Although introducing sparse priors in imaging methods can suppress sidelobes to a certain extent under different SNR, the loss of target structural information in the imaging results makes it difficult to support subsequent image interpretation. Compared with such methods, the proposed method introduces composite priors and more effectively reconstructs the structural information of the target. Table 2 presents the quantitative evaluation indicators for various methods with different SNR. The NMSE of the proposed method was 0.0492, 0.0554, and 0.0737 at SNR of 15 dB, 10 dB, and 5 dB, respectively. The SSIM of CP-VSAM was 0.9888, 0.9834, and 0.9696 at SNR of 15 dB, 10 dB, and 5 dB, respectively. As the SNR decreased, although the performance of CP-VSAM decreased, it still outperformed methods such as $L_1$, LR-$L_1$, and SCAD.

### *4.2. The Experiment of the Metal Hammer*

To validate the method's effectiveness in practical applications, an experiment involving metal hammer targets was conducted. Figure 8a depicts the experimental setup, while the main parameters are outlined below: the signal's bandwidth was 3.599 GHz, with a center frequency of 78.8 GHz, and the scanning range of the array set in the experiment was 0.4 m $\times$ 0.4 m.

**Table 2.** The NMSE and SSIM for aircraft imaging under varying SNR.

| SNR | $L_1$ | | | SCAD | | | LR-$L_1$ | | | CP-VSAM | | |
|---|---|---|---|---|---|---|---|---|---|---|---|---|
| | NMSE | SSIM | PSNR | NMSE | SSIM | PSNR | NMSE | SSIM | PSNR | NMSE | SSIM | PSNR |
| 15 dB | 0.3432 | 0.9034 | 41.9260 | 0.1692 | 0.9378 | 45.6580 | 0.1210 | 0.9784 | 46.4538 | 0.0492 | 0.9888 | 47.5686 |
| 10 dB | 0.3482 | 0.8853 | 41.8101 | 0.1759 | 0.9210 | 45.4354 | 0.1270 | 0.9680 | 46.4270 | 0.0554 | 0.9834 | 47.1349 |
| 5 dB | 0.3659 | 0.8453 | 41.4871 | 0.1979 | 0.8826 | 44.8170 | 0.1435 | 0.9514 | 46.2578 | 0.0737 | 0.9696 | 47.7836 |

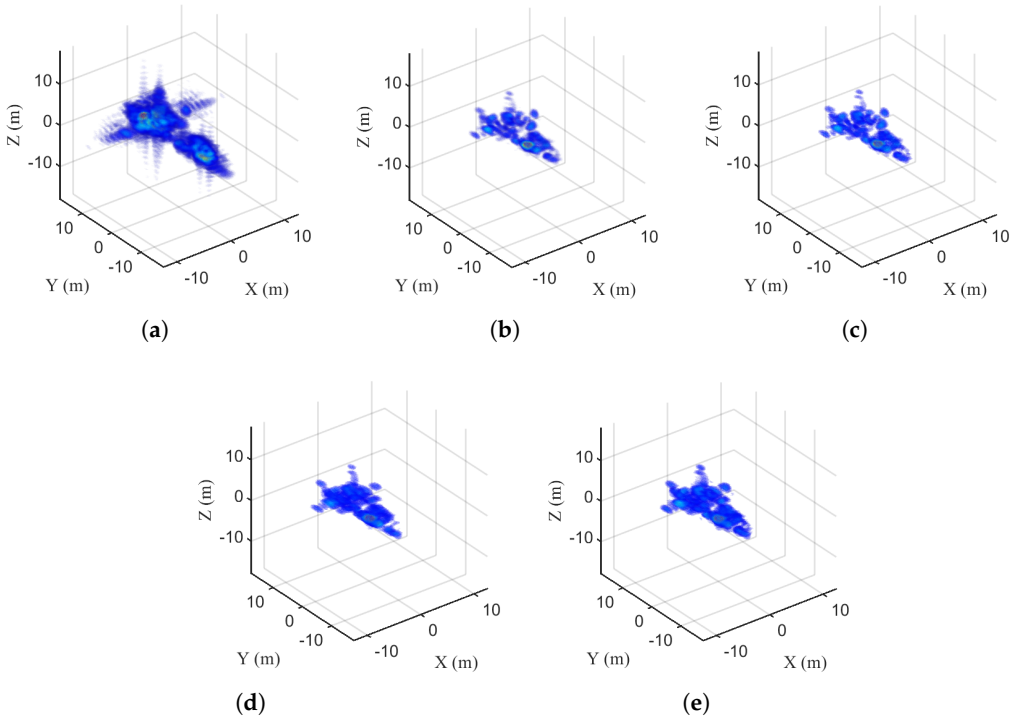



**Figure 6.** Aircraft target imaging results under 10 dB SNR. (**a**) MFW. (**b**) $L_1$. (**c**) SCAD. (**d**) LR$-L_1$. (**e**) CP-VSAM.

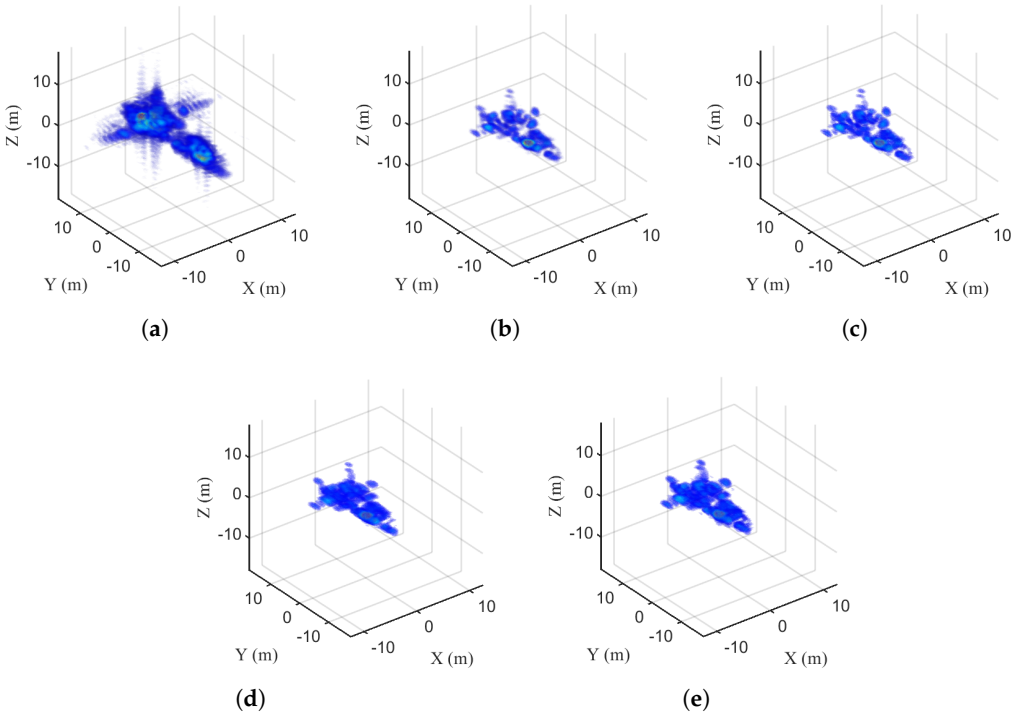
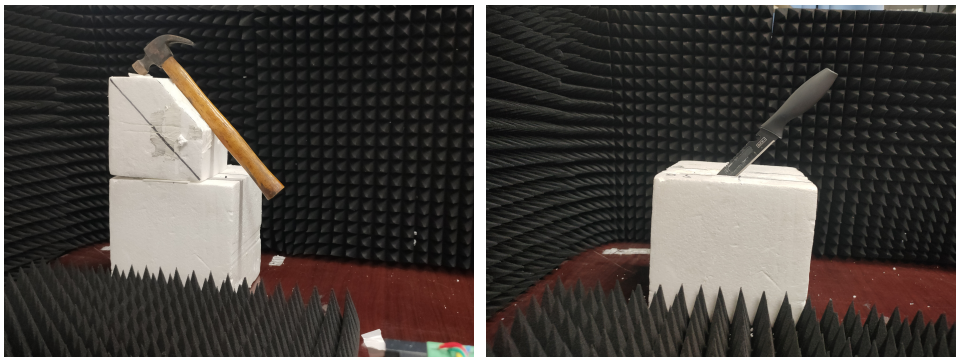



**Figure 7.** Aircraft target imaging results under 5 dB SNR. (**a**) MFW. (**b**) $L_1$. (**c**) SCAD. (**d**) LR$-L_1$. (**e**) CP-VSAM.



(**a**) (**b**)

**Figure 8.** The target scene. (**a**) The metal hammer. (**b**) The metal stiletto.

Figures 9–11 display the imaging results obtained under varying SR conditions. The 3D imaging results indicate that there were still significant sidelobes in the images obtained by the MF imaging method under full sampling conditions, and the images appeared more blurry as the sampling rate decreased. It can be easily seen from the target handle in the red box that the sparse driving method caused a significant loss in the details and texture information of this part. Compared to this, the SLRP driven method can improve this phenomenon. However, LR-$L_1$ introduces reconstruction bias and still loses information. To further reconstruct the detailed information of the handle part of the target, the proposed method achieves more accurate reconstruction of the target by integrating non-convex regularization functions and INN. Although sparse driven methods such as $L_1$, LR-$L_1$, and SCAD can suppress sidelobes, these only consider the sparse features of the target and lose non-sparse structural information, which can affect image interpretation and scattering information measurement.

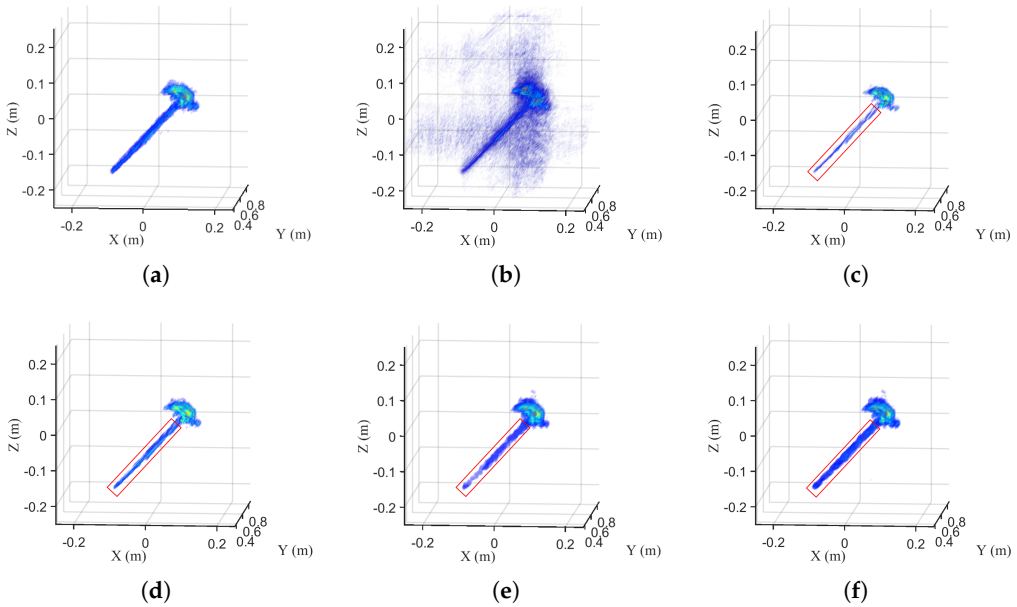



**Figure 9.** The imaging result of the hammer under 100% SR. (**a**) RI. (**b**) MFW. (**c**) $L_1$. (**d**) SCAD. (**e**) LR-$L_1$. (**f**) CP-VSAM.

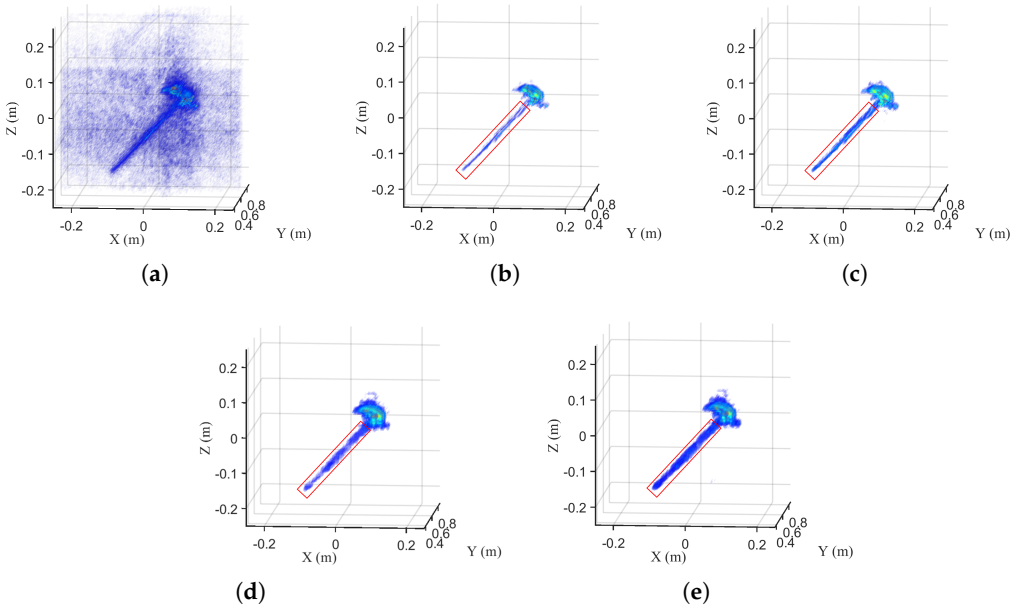



**Figure 10.** The imaging result of the hammer under 75% SR. (**a**) MFW. (**b**) $L_1$. (**c**) SCAD. (**d**) LR$-L_1$. (**e**) CP-VSAM.

Comparatively, CP-VSAM can still achieve high-quality imaging even with limited observation data, and the information of the target in 3D space is more complete, verifying the effectiveness of CP-VSAM. Specifically, the proposed method achieves more effective 3D reconstruction of complex targets by exploring composite priors. In Table 3, a numerical analysis of various methods is provided. Under 100% sampling, the NMSE of $L_1$, SCAD, LR-$L_1$, and CP-VSAM were 0.4393, 0.2734, 0.1474, and 0.0970, respectively. The SSIMs of $L_1$, SCAD, LR-$L_1$, and CP-VSAM were 0.4620, 0.5804, 0.9001 and 0.9382, respectively.

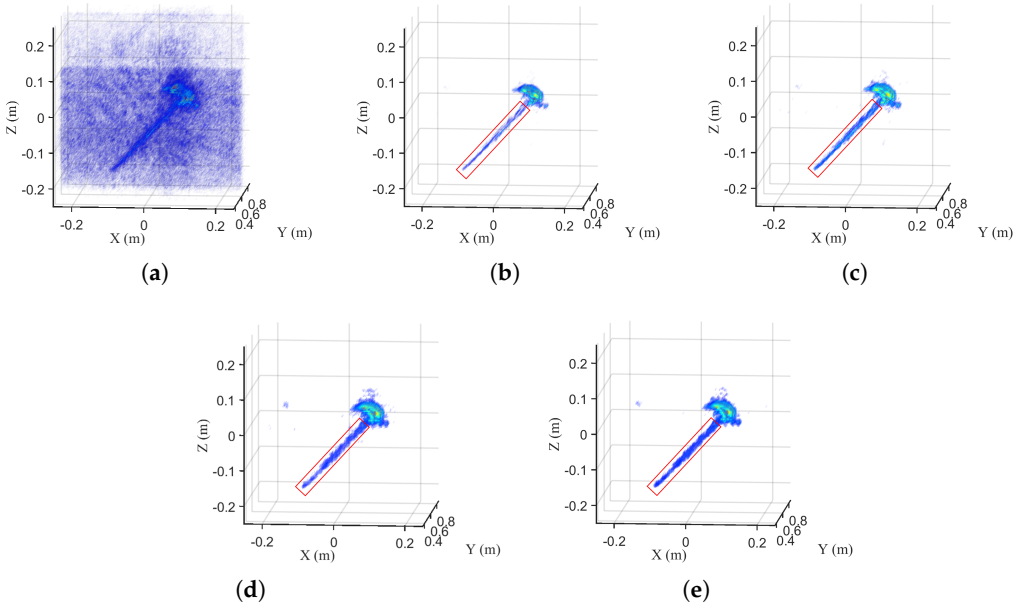



**Figure 11.** The imaging result of the hammer under 50% SR. (**a**) MFW. (**b**) $L_1$. (**c**) SCAD. (**d**) LR$-L_1$. (**e**) CP-VSAM.

**Table 3.** NMSE and SSIM of metal hammer imaging under different SR conditions.

| SR | $L_1$ | | | SCAD | | | LR-$L_1$ | | | CP-VSAM | | |
|---|---|---|---|---|---|---|---|---|---|---|---|---|
| | NMSE | SSIM | PSNR | NMSE | SSIM | PSNR | NMSE | SSIM | PSNR | NMSE | SSIM | PSNR |
| 100% | 0.4393 | 0.4620 | 32.5961 | 0.2734 | 0.5804 | 35.6321 | 0.1474 | 0.9001 | 37.5371 | 0.0970 | 0.9382 | 38.6813 |
| 75% | 0.5530 | 0.2997 | 31.1016 | 0.4146 | 0.3970 | 33.5409 | 0.1808 | 0.8838 | 35.1743 | 0.1166 | 0.9313 | 36.7941 |
| 50% | 0.6676 | 0.1888 | 29.0568 | 0.5447 | 0.2778 | 31.0980 | 0.2026 | 0.8683 | 33.4990 | 0.1691 | 0.8929 | 34.9618 |

### *4.3. The Experiment of the Metal Stiletto*

To further weigh the performance of CP-VSAM, another set of SAR data was processed, with the target scene illustrated in Figure 8b. The visualization results at different SR are shown in Figures 12–14. It can be seen that at different SR, the results of MF exhibited varying degrees of blurring, which affected image interpretation. The proposed method was shown to effectively reconstruct target information at different SR and suppress sidelobes and clutter, significantly improving imaging quality. The corresponding numerical analysis is listed in Table 4, which indicates that CP-VSAM exhibited superior 3D SAR imaging performance across various sampling conditions. At 50% sampling, the NMSE and SSIM of CP-VSAM weare 0.1713 and 0.8085, respectively. CP-VSAM continued to outperform comparison sparse driving methods in terms of imaging performance, with NMSE reduced by about two times and SSIM increased by about two times. The analysis results demonstrate that CP-VSAM is capable of effectively reconstructing complex targets in real scenarios while preserving the structural information of the targets.

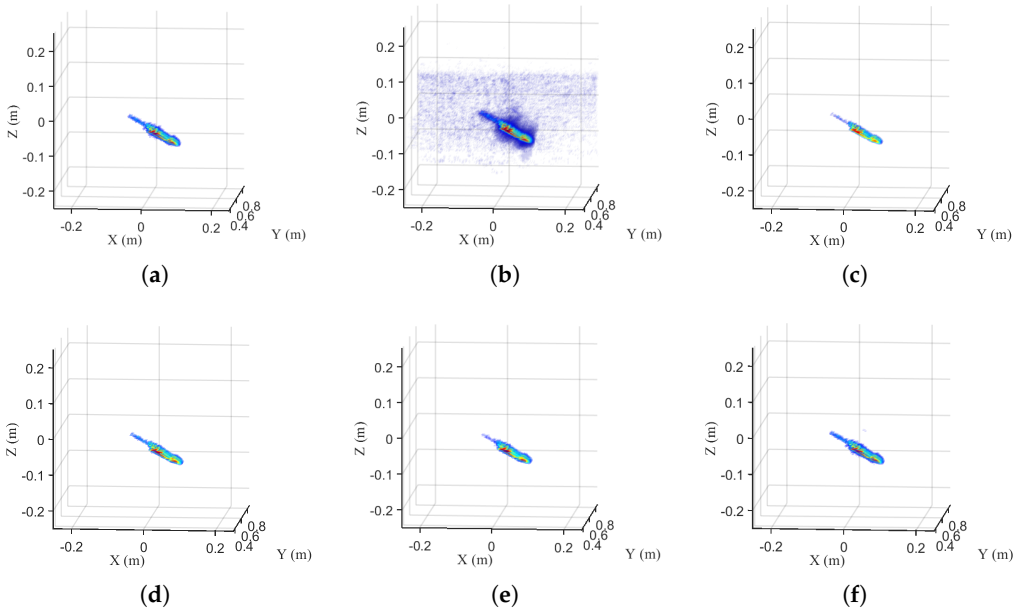



**Figure 12.** The imaging result of the stiletto under 100% SR. (**a**) RI. (**b**) MFW. (**c**) $L_1$. (**d**) SCAD. (**e**) LR$-L_1$. (**f**) CP-VSAM.

**Table 4.** NMSE and SSIM of metal stiletto imaging under different SR conditions.

| SR | $L_1$ | | | SCAD | | | LR-$L_1$ | | | CP-VSAM | | |
|---|---|---|---|---|---|---|---|---|---|---|---|---|
| | NMSE | SSIM | PSNR | NMSE | SSIM | PSNR | NMSE | SSIM | PSNR | NMSE | SSIM | PSNR |
| 100% | 0.5498 | 0.5685 | 34.9562 | 0.3291 | 0.6468 | 38.5992 | 0.1773 | 0.8663 | 39.1980 | 0.1471 | 0.9059 | 40.2231 |
| 75% | 0.6382 | 0.4322 | 33.7066 | 0.4019 | 0.4991 | 36.7027 | 0.2090 | 0.8002 | 38.0341 | 0.1575 | 0.8315 | 39.6709 |
| 50% | 0.7410 | 0.2782 | 31.4456 | 0.5299 | 0.3350 | 33.8682 | 0.2232 | 0.7663 | 36.3580 | 0.1713 | 0.8085 | 37.0862 |

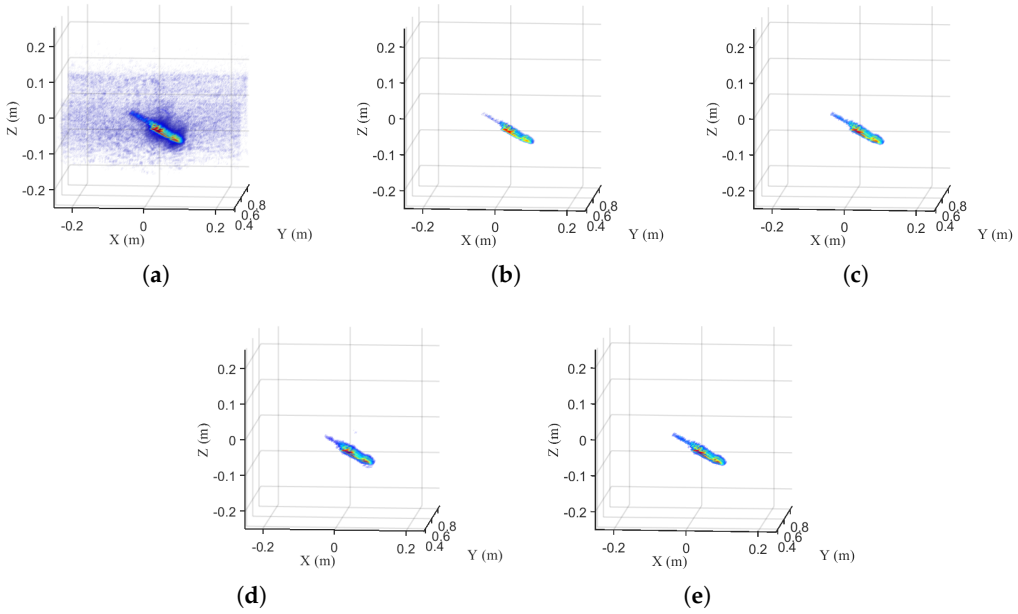



**Figure 13.** The imaging result of the stiletto under 75% SR. (**a**) MFW. (**b**) $L_1$. (**c**) SCAD. (**d**) LR$-L_1$. (**e**) CP-VSAM.

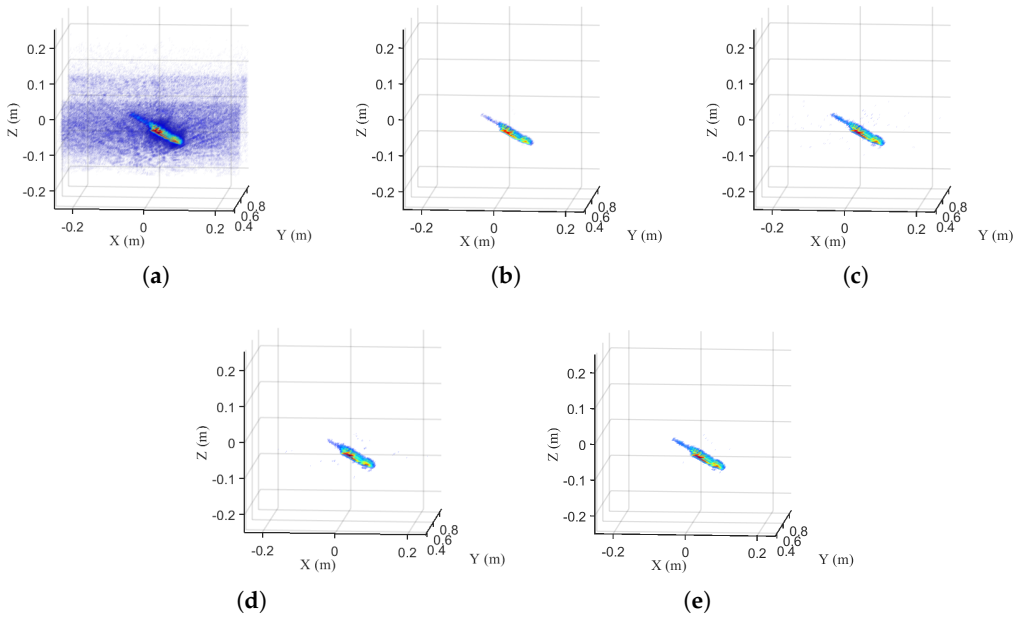


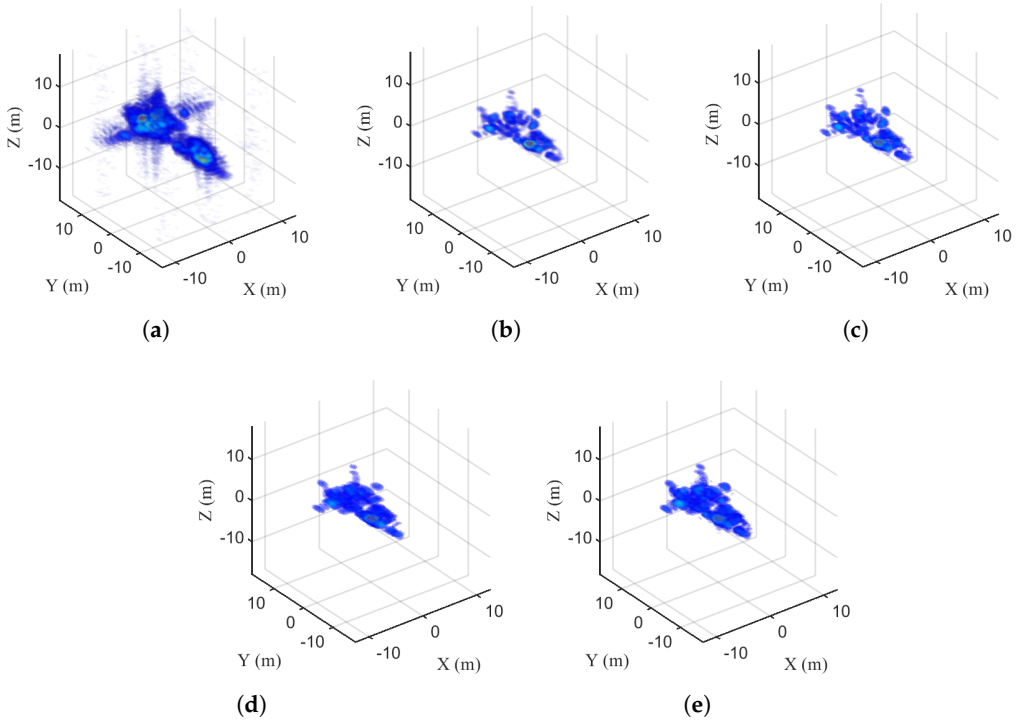

**Figure 14.** The imaging result of the stiletto under 50% SR. (**a**) MFW. (**b**) $L_1$. (**c**) SCAD. (**d**) LR$-L_1$. (**e**) CP-VSAM.

## 5. Discussion

We performed imaging processing on aircraft models with lower SNR (0 dB and $-5$ dB) to further validate the effectiveness of the proposed method. Figures 15 and 16 show the imaging results under 0 dB and $-5$ dB SNR conditions, respectively. From the visualization results, it can be seen the proposed method can effectively reconstruct the target. Furthermore, the corresponding numerical analysis is listed in Table 5. At 0 dB, the NMSE of $L_1$, SCAD, LR-$L_1$, and CP VSAM were 0.4146, 0.2596, 0.1922, and 0.1262, respectively. The SSIM of $L_1$, SCAD, LR-$L_1$, and CP VSAM were 0.7550, 0.7941, 0.9098, and 0.9377, respectively. Under the condition of $-5$ dB, although the performance of the proposed method decreased, it still outperformed other comparative methods.

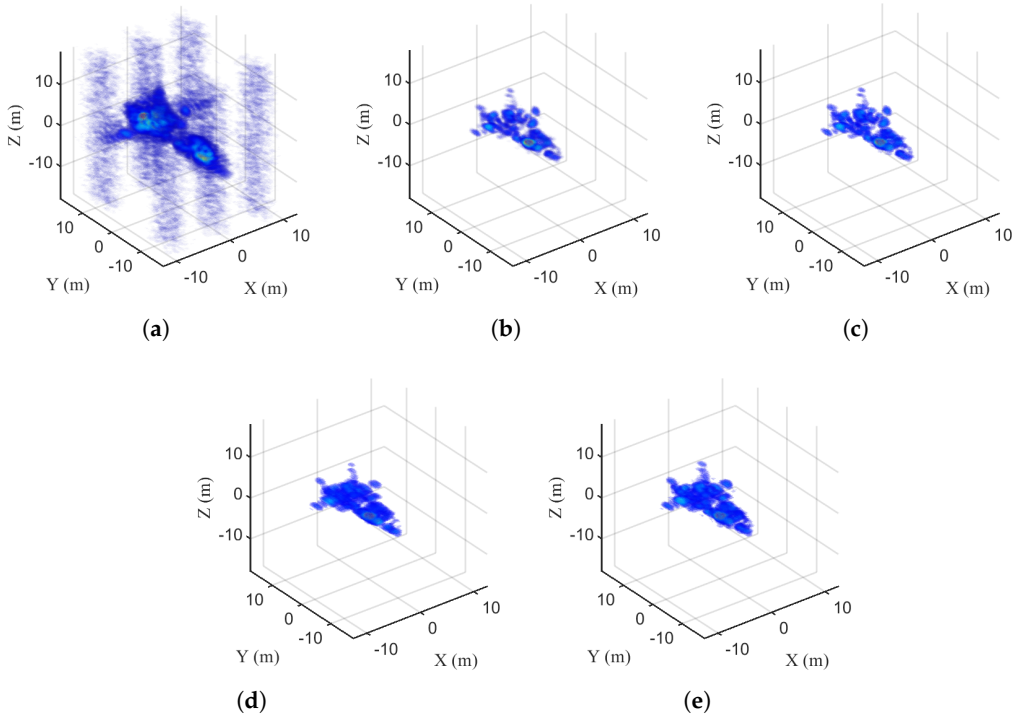
**Table 5.** The NMSE and SSIM for aircraft imaging under low SNR.

| SNR | $L_1$ | | | SCAD | | | LR-$L_1$ | | | CP-VSAM | | |
|---|---|---|---|---|---|---|---|---|---|---|---|---|
| | NMSE | SSIM | PSNR | NMSE | SSIM | PSNR | NMSE | SSIM | PSNR | NMSE | SSIM | PSNR |
| 0 dB | 0.4146 | 0.7550 | 40.5800 | 0.2596 | 0.7941 | 43.2745 | 0.1922 | 0.9098 | 45.9394 | 0.1262 | 0.9377 | 46.8744 |
| −5 dB | 0.5263 | 0.5787 | 38.4967 | 0.4018 | 0.6174 | 40.3295 | 0.2979 | 0.8221 | 45.0918 | 0.2426 | 0.8554 | 46.2178 |




(**a**) (**b**) (**c**) (**d**) (**e**)

**Figure 15.** Aircraft target imaging results under 0 dB SNR. (**a**) MFW. (**b**) $L_1$. (**c**) SCAD. (**d**) LR−$L_1$. (**e**) CP-VSAM.




(**a**) (**b**) (**c**) (**d**) (**e**)

**Figure 16.** Aircraft target imaging results under −5 dB SNR. (**a**) MFW. (**b**) $L_1$. (**c**) SCAD. (**d**) LR−$L_1$. (**e**) CP-VSAM.

## 6. Conclusions

Existing array 3D SAR imaging usually only introduces sparse priors of the target scene, resulting in loss of target information or even reconstruction failure in the 3D imaging space under limited observation data. In response to this issue, in this article. a new array 3D SAR imaging framework based on non-convex regularization functions and INN is proposed, which can achieve effective target reconstruction from limited observation data. Specifically, by constructing a composite imaging optimization model, the composite representation of target features can be achieved, which more effectively reconstruct the information of the target in 3D space. CP-VSAM more effectively characterizes the composite features of targets in 3D space and significantly improves imaging quality compared to imaging methods with sparse driving. Additionally, to solve the optimization problem of composite imaging, we propose a framework that integrates variable splitting and alternative minimization, which can effectively reconstruct high-dimensional imaging scenes. Finally, the majority of simulations and actual experiments are conducted to investigate the performance of CP-VSAM. The visualization results and quantitative analysis indicate that CP-VSAM can achieve high-quality 3D SAR imaging with limited observation data, providing support for subsequent image interpretation and target scattering diagnosis. Considering that low-rank and sparse priors may not be sufficient to fully adapt to certain highly complex or extreme scattering characteristics, in the future, the proposed framework can explore the introduction of diverse priors and combining multi-source data to further enhance the adaptability of the method to complex scenarios.

**Author Contributions:** The main conceptual contributions of this article are Z.Y. and Y.W. The validation was mainly carried out by Y.W., X.Z. and C.Z. The writing was mainly completed by Z.Y. and Y.W. The visualization of this article was mainly performed by Y.W. and Y.L. The supervision was mainly conducted by Y.W. and G.S. The project administration was mainly performed by Y.W., G.S., and Y.M. All authors have read and agreed to the published version of the manuscript.

**Funding:** This research was supported in part by the National Natural Science Foundation of China under Grant 62401518; in part by the Sichuan Science and Technology Program under Grant 2023NSFSC1382; and in part by the Fundamental Research Program of Shanxi Province under Grant 202203021212141.

**Data Availability Statement:** The original contributions presented in the study are included in the article, further inquiries can be directed to the corresponding author.

**Acknowledgments:** The authors would like to thank all reviewers and editors for their comments on this paper.

**Conflicts of Interest:** The authors declare no conflicts of interest.

## References

1. Moreira, A.; Prats-Iraola, P.; Younis, M.; Krieger, G.; Hajnsek, I.; Papathanassiou, K.P. A Tutorial on Synthetic Aperture Radar. *IEEE Geosci. Remote Sens. Mag.* **2013**, *1*, 6–43. [CrossRef]
2. Xu, Z.; Liu, M.; Zhou, G.; Wei, Z.; Zhang, B.; Wu, Y. An Accurate Sparse SAR Imaging Method for Enhancing Region-Based Features via Nonconvex and TV Regularization. *IEEE J. Sel. Top. Appl. Earth Observ. Remote Sens.* **2021**, *14*, 350–363. [CrossRef]
3. Zhou, L.; Deng, M.; He, J.; Wang, B.; Zhang, S.; Liu, X.; Wei, S. A HRWS SAR Motion Compensation Method With Multichannel Phase Correction. *Remote Sens.* **2024**, *16*, 3544. [CrossRef]
4. Wang, Z.; Guo, Q.; Tian, X. 3D Millimeter-wave Imaging Using MIMO RMA with Range Compensation. *IEEE Trans. Microw. Theory Tech.* **2019**, *67*, 1157–1166. [CrossRef]
5. Dang, S.; Cui, Z.; Cao, Z.; Liu, N. SAR Target Recognition via Incremental Nonnegative Matrix Factorization. *Remote Sens.* **2018**, *10*, 374. [CrossRef]
6. Wang, Y.; Zhang, X.; Zhan, X.; Zhang, T.; Zhou, L.; Shi, J.; Wei, S. An RCS Measurement Method Using Sparse Imaging Based 3D SAR Complex Image. *IEEE Antennas Wirel. Propag. Lett.* **2022**, *21*, 24–28. [CrossRef]

7. Wang, Y.; Zhan, X.; Yao, J.; Zhan, Y.; Bai, J. 3D Sparse SAR Imaging Based on Complex-Valued Nonconvex Regularization for Scattering Diagnosis. *IEEE Antennas Wirel. Propag. Lett.* **2024**, *23*, 888–892. [CrossRef]
8. Zeng, T.; Zhan, X.; Ma, X.; Liu, R.; Shi, J.; Wei, S. Unsupervised 3D Array-SAR Imaging Based on Generative Model for Scattering Diagnosis. *IEEE Antennas Wirel. Propag. Lett.* **2024**, *23*, 2451–2455. [CrossRef]
9. Wang, M.; Wei, S.; Liang, J.; Liu, S.; Shi, J.; Zhang, X. Lightweight FISTA-Inspired Sparse Reconstruction Network for mmW 3D Holography. *IEEE Trans. Geosci. Remote Sens.* **2022**, *60*, 5211620.
10. Wang, M.; Wei, S.; Zhou, Z.; Shi, J.; Zhang, X.; Guo, Y. 3D SAR Autofocusing with Learned Sparsity. *IEEE Trans. Geosci. Remote Sens.* **2022**, *60*, 5235818.
11. Wei, S.; Zhou, Z.; Wang, M.; Wei, J.; Liu, S.; Shi, J.; Zhang, X.; Fan, F. 3DRIED: A High-Resolution 3D Millimeter-Wave Radar Dataset Dedicated to Imaging and Evaluation. *Remote Sens.* **2021**, *13*, 3366. [CrossRef]
12. Tian, B.; Zhang, X.; Li, L.; Pu, L.; Pu, L.; Shi, J.; Wei, S. Fast Bayesian Compressed Sensing Algorithm via Relevance Vector Machine for LASAR 3D Imaging. *Remote Sens.* **2021**, *13*, 1751. [CrossRef]
13. Wang, L.; Yao, X.; Song, T.; Wang, Y.; Sun, G. An Elliptical Bipolar Cylindrical Coordinates Based Mixed Domain Near-Field Imaging Algorithm for Scanning 1-D Nonuniform Sparse MIMO Arrays. *IEEE Trans. Geosci. Remote Sens.* **2024**, *62*, 5208814.
14. Xu, G.; Chen, Y.; Ji, A.; Zhang, B.; Yu, C.; Hong, W. 3D High-Resolution Imaging and Array Calibration of Ground-Based Millimeter-Wave MIMO Radar. *IEEE Trans. Microw. Theory Tech.* **2024**, *72*, 4919–4931. [CrossRef]
15. Alvarez, J. Near-Field 2-D-lateral Scan System for RCS Measurement of Full-Scale Targets Located on the Ground. *IEEE Trans. Antennas Propag.* **2019**, *67*, 4049–4058. [CrossRef]
16. Tulgar, O.; Ergin, A.A. Improved Pencil Back-Projection Method With Image Segmentation for Far-Field/Near-Field SAR Imaging and RCS Extraction. *IEEE Trans. Antennas Propag.* **2015**, *63*, 2572–2584. [CrossRef]
17. Xu, Z.; Zhang, B.; Zhou, G.; Zhong, L.; Wu, Y. Sparse SAR Imaging and Quantitative Evaluation Based on Nonconvex and TV Regularization. *Remote Sens.* **2021**, *13*, 1643. [CrossRef]
18. Karakus, O.; Mayo, P.; Achim, A. Convergence Guarantees for Nonconvex Optimisation With Cauchy-based Penalties. *IEEE Trans. Signal Process.* **2020**, *68*, 6159–6170. [CrossRef]
19. Gao, J.; Wang, Y.; Yao, J.; Zhan, X.; Sun, G.; Bai, J. Three-Dimensional Array SAR Sparse Imaging Based on Hybrid Regularization. *IEEE Sens. J.* **2024**, *24*, 16699–16709. [CrossRef]
20. Bi, H.; Wang, J.; Bi, G. Wavenumber Domain Algorithm-Based FMCW SAR Sparse Imaging. *IEEE Trans. Geosci. Remote Sens.* **2019**, *57*, 7466–7475. [CrossRef]
21. Peng, X.; Tan, W.; Hong, W.; Jiang, C.; Bao, Q.; Wang, Y. Airborne DLSLA 3D SAR Image Reconstruction by Combination of Polar Formatting and $L_1$ Regularization. *IEEE Trans. Geosci. Remote Sens.* **2016**, *54*, 213–226. [CrossRef]
22. Yao, J.; Meng, D.; Zhao, Q.; Cao, W.; Xu, Z. Nonconvex-Sparsity and Nonlocal-Smoothness-Based Blind Hyperspectral Unmixing. *IEEE Trans. Image Process.* **2019**, *28*, 2991–3006. [CrossRef] [PubMed]
23. Wang, Y.; He, Z.; Zhan, X.; Zeng, Q.; Hu, Y. A 3D Sparse SAR Imaging Method Based on Plug-and-Play. *IEEE Trans. Geosci. Remote Sens.* **2022**, *60*, 5238514. [CrossRef]
24. Karakuş, O.; Achim, A. On Solving SAR Imaging Inverse Problems Using Nonconvex Regularization with A Cauchy-Based Penalty. *IEEE Trans. Geosci. Remote Sens.* **2020**, *59*, 5828–5840. [CrossRef]
25. Zuo, W.; Meng, D.; Zhang, L.; Feng, X.; Zhang, D. A Generalized Iterated Shrinkage Algorithm for Non-convex Sparse Coding. In Proceedings of the 2013 IEEE International Conference on Computer Vision, Sydney, NSW, Australia, 1–8 December 2013; pp. 217–224.
26. Wang, Y.; He, Z.; Zhan, X.; Fu, Y.; Zhou, L. Three-Dimensional Sparse SAR Imaging with Generalized $L_q$ Regularization. *Remote Sens.* **2022**, *14*, 288. [CrossRef]
27. Fan, J.; Li, R. Variable Selection via Nonconcave Penalized Likelihood and Its Oracle Properties. *J. Am. Stat. Assoc.* **2001**, *96*, 1348–1360. [CrossRef]
28. Xu, Z. $L_{1/2}$ Regularization: A Thresholding Representation Theory and a Fast Solver. *IEEE Trans. Neural Netw. Learn. Syst.* **2012**, *23*, 1013–1027.
29. Zhang, C.-H. Nearly Unbiased Variable Selection Under Minimax Concave Penalty. *Ann. Statist.* **2010**, *38*, 894–942. [CrossRef]
30. Daubechies, I.; Defriese, M.; De Mol, C. An Iterative Thresholding Algorithm for Linear Inverse Problems with A Sparsity Constraint. *Commun. Pure Appl. Math.* **2004**, *57*, 1413–1457. [CrossRef]
31. Boyd, S.; Parikh, N.; Chu, E.; Peleato, B.; Eckstein, J. Distributed Optimization and Statistical Learning via The Alternating Direction Method of Multipliers. *Found. Trends® Mach. Learn.* **2011**, *3*, 128.
32. Afonso, M.V.; Bioucas-Dias, J.-M.; Figueiredo, M.A.T. Fast Image Recovery Using Variable Splitting and Constrained Optimization. *IEEE Trans. Image Process.* **2010**, *19*, 2345–2356. [CrossRef] [PubMed]
33. Donoho, D.L.; Maleki, A.; Montanari, A. Message-Passing Algorithms for Compressed Sensing. *Proc. Nat. Acad. Sci. USA* **2009**, *106*, 18914–18919. [CrossRef] [PubMed]

34. Cheng, K.; Du, J.; Zhou, H.; Zhao, D.; Qin, H. Image Super-Resolution Based on Half Quadratic Splitting. *Infrared Phys. Technol.* **2020**, *105*, 103193. [CrossRef]
35. Liao, X.; Li, H.; Carin, L. Generalized Alternating Projection for Weighted-$l_{2,1}$ Minimization with Applications to Model-Based Compressive Sensing. *SIAM J. Imag. Sci.* **2014**, *7*, 797–823. [CrossRef]
36. Wei, Z.; Zhang, B.; Xu, Z.; Han, B.; Hong, W.; Wu, Y. An Improved SAR Imaging Method Based on Nonconvex Regularization and Convex Optimization. *IEEE Geosci. Remote Sens. Lett.* **2019**, *16*, 1580–1584. [CrossRef]
37. Bi, H.; Lu, X.; Yin, Y.; Yang, W.; Zhu, D. Sparse SAR Imaging Based on Periodic Block Sampling Data. *IEEE Trans. Geosci. Remote Sens.* **2022**, *60*, 5213812. [CrossRef]
38. Dou, Y.Y.; Wu, Y.M.; Jin, H.Q.; Jin, Y.-Q.; Hu, J.; Cheng, J. The Efficient Norm Regularization Method Applying on The ISAR Image with Sparse Data. *IEEE Trans. Geosci. Remote Sens.* **2022**, *60*, 5237711. [CrossRef]
39. Bi, H.; Feng, J.; Jin, S.; Yang, W.; Xu, W. Mixed-Norm Regularization-Based Polarimetric Holographic SAR 3D Imaging. *IEEE Geosci. Remote Sens. Lett.* **2024**, *21*, 4002305. [CrossRef]
40. Wu, A.; Wu, Y.; Jin, Y.; Wang, Y.; Guo, Z. $L_{1/2}$ Regularization for ISAR Imaging and Target Enhancement of Complex Image. *IEEE Trans. Geosci. Remote Sens.* **2022**, *60*, 5200410.
41. Wang, Y.; He, Z.; Yang, F.; Zeng, Q.; Zhan, X. 3D Sparse SAR Image Reconstruction Based on Cauchy Penalty and Convex Optimization. *Remote Sens.* **2022**, *14*, 2308. [CrossRef]
42. Pu, W.; Wang, X.; Wu, J.; Huang, Y.; Yang, J. Video SAR Imaging Based on Low-Rank Tensor Recovery. *IEEE Trans. Neural Netw. Learn. Syst.* **2021**, *32*, 188–202. [CrossRef] [PubMed]
43. Selesnick, I. Sparse Regularization Via Convex Analysis. *IEEE Trans. Signal Process.* **2017**, *65*, 4481–4494. [CrossRef]
44. Liu, Q.; Li, X. Efficient Low-Rank Matrix Factorization Based on l 1, $\varepsilon$-Norm for Online Background Subtraction. *IEEE Trans. Circuits. Syst. Video Technol.* **2022**, *32*, 4900–4904. [CrossRef]
45. Zhang, Z.; Aeron, S. Exact Tensor Completion Using T-SVD. *IEEE Trans. Signal Process.* **2017**, *65*, 1511–1526. [CrossRef]
46. Zhang, C.; Fu, H.; Hu, Q.; Cao, X.; Xie, Y.; Tao, D. Generalized Latent Multi-View Subspace Clustering. *IEEE Trans. Pattern Anal. Mach. Intell.* **2020**, *42*, 86–99. [CrossRef]
47. Prakash, J.; Sanny, D.; Kalva, S.K.; Pramanik, M.; Yalavarthy, P.K. Fractional Regularization to Improve Photoacoustic Tomographic Image Reconstruction. *IEEE Trans. Med. Imaging* **2019**, *38*, 1935–1947. [CrossRef]
48. Fang, J.; Xu, Z.; Zhang, B.; Hong, W.; Wu, Y. Fast Compressed Sensing SAR Imaging Based on Approximated Observation. *IEEE J. Sel. Top. Appl. Earth Observ. Remote Sens.* **2014**, *7*, 352–363. [CrossRef]
49. Chen, X.; Luo, C.; Yang, Q.; Yang, L.; Wang, H. Efficient MMW image Reconstruction Algorithm Based on ADMM Framework for Near-Field MIMO-SAR. *IEEE Trans. Microw. Theory Tech.* **2023**, *72*, 1326–1338. [CrossRef]
50. Roberts, W.; Stoica, P.; Li, J.; Yardibi, T.; Sadjadi, F.A. Iterative Adaptive Approaches to MIMO Radar Imaging. *IEEE J. Sel. Top. Appl. Earth Observ. Remote Sens.* **2010**, *4*, 5–20. [CrossRef]
51. Zeng, T.; Zhan, X.; Ren, Y.; Ma, X.; Liu, L.; Shi, J.; Wei, S.; Wang, M.; Zhang, X. Exploring Spatial Feature Regularization in Deep-Learning-Based TomoSAR Reconstruction: A Preliminary Study and Performance Analysis. *IEEE Trans. Geosci. Remote Sens.* **2024**, *63*, 5201227. [CrossRef]
52. Fan, Y.; Wang, K.; Li, J.; Zhou, G.; Zhang, B.; Wu, Y. L-hypersurface Based Parameters Selection in Composite Regularization Models with Application to SAR and Tomosar Imaging. *IEEE J. Sel. Top. Appl. Earth Obs. Remote Sens.* **2023**, *16*, 8297–8309. [CrossRef]
53. Fan, Y.; Zhang, B.; Wu, Y. Integrating Regularization and PnP Priors for SAR Image Reconstruction Using Multiagent Consensus Equilibrium. *IEEE Trans. Geosci. Remote Sens.* **2024**, *62*, 5228115. [CrossRef]


**Disclaimer/Publisher's Note:** The statements, opinions and data contained in all publications are solely those of the individual author(s) and contributor(s) and not of MDPI and/or the editor(s). MDPI and/or the editor(s) disclaim responsibility for any injury to people or property resulting from any ideas, methods, instructions or products referred to in the content.